Serbena, Francisco Carlos; Foerster, Carlos Eugênio; Jurelo, Alcione Roberto; Mikowski, Alexandre;
Rodrigues Júnior, Pedro; Carubelli, Célia Regina; Lepienski, Carlos Maurício

Depth-Sensing Indentation on REBa2Cu3O7- Single Crystals Obtained from Xenotime Mineral

SBF
SOCIEDADE BRASILEIRA DE FÍSICA

CONDENSED MATTER

Depth-Sensing Indentation on REBa₂Cu₃O₇₋δ Single Crystals Obtained from Xenotime Mineral

Francisco Carlos Serbena · Carlos Eugênio Foerster ·
Alcione Roberto Jurelo · Alexandre Mikowski ·
Pedro Rodrigues Júnior · Célia Regina Carubelli ·
Carlos Maurício Lepienski

Abstract A natural mixture of heavy rare-earth oxides extracted from xenotime mineral have been used to prepare large single crystals of the high-temperature REBa₂Cu₃O₇₋δ superconductor, grown using the CuO–BaO self-flux method. Its mechanical properties along the *ab*-plane were characterized using instrumented indentation. Hardness and elastic moduli were measured by the Oliver and Pharr method, which yielded 7.4±0.2 GPa and the range 135–175 GPa at small depths, respectively. Increased loads promote the nucleation of lateral cracks, which reduce hardness and measured elastic modulus, as indicated by instrumented indentation at higher loads. The indentation fracture toughness, estimated by measuring the radial crack length from cube corner indentations at various loads, was found to be 0.8±0.2 MPa m$^{1/2}$. The observed slip systems of REBa₂Cu₃O₇₋δ single crystals were [100](001) and [010](001), the same as for YBa₂Cu₃O₇₋δ single crystals. The initial stages of deformation and fracture in the indentation process were investigated. The hardness and elastic modulus are not strongly modified by the crystallographic orientation in the *ab*-plane. This was interpreted in terms of resolved shear stresses in the active slip systems. Evidence of cracking along the {100} and {110} planes on the *ab*-plane was observed. In conclusion, the mechanical properties of REBa₂Cu₃O₇₋δ single crystals prepared from xenotime are equivalent to those of YBa₂Cu₃O₇₋δ single crystals from conventional rare-earth oxides.

Keywords High-temperature superconductors · Single crystal · Xenotime · Mechanical properties

F. C. Serbena (✉) · C. E. Foerster · A. R. Jurelo · P. R. Júnior
Departamento de Física, Universidade Estadual de Ponta Grossa,
Av. Gen. Carlos Cavalcanti 4748, Campus de Uvaranas,
84.030-000 Ponta Grossa, Paraná, Brazil
e-mail: fserbena@uepg.br

A. Mikowski
Centro de Engenharia da Mobilidade, Universidade Federal de
Santa Catarina,
Campus Universitário, Bairro Bom Retiro, Caixa Postal 246,
89.219-905 Joinville, Santa Catarina, Brazil

C. R. Carubelli
Departamento de Química, Universidade Estadual de Ponta
Grossa,
Av. Gen. Carlos Cavalcanti 4748, Campus de Uvaranas,
84.030-000 Ponta Grossa, Paraná, Brazil

C. M. Lepienski
Departamento de Física, Universidade Federal do Paraná,
Cx. Postal 19044, 81531-990 Curitiba, Paraná, Brazil

1 Introduction

Rare earth elements play an important role in energy production technological materials, such as high-energy density materials and high-temperature superconductor generators. Recently, they have become increasingly more expensive due to limited global supply, which led to escalating costs for energy technologies associated with them. Yttrium has been recognized as one of the most important rare earth elements for clean energy applications and lies among those with the highest supply risk in the medium term [1]. Therefore, there is a demand for new technologies and materials that can reduce production cost by developing alternatives to the conventional methods with comparable performance.

It is known that minerals such as monazite, bastnäsite, and xenotime are sources for such rare earth elements as the lanthanides and yttrium [2]. Particularly, xenotime is a mixture of phosphates of yttrium and heavy lanthanides (ranging from gadolinium to lutetium), from which a natural mixture of rare earth trivalent oxides and Y can be extracted. This provide an alternative, nonexpensive route to prepare a

high T_c superconductor isostructural to $YBa_2Cu_3O_{7-\delta}$ in low demand of high purity yttrium or other pure lanthanide element on the Y site. Polycrystalline, melt-textured, and single-crystal samples using rare earth elements extracted from xenotime have been successfully grown, with good superconductor properties [3–5].

Large, good quality single crystals of high-temperature superconductors are required for highly accurate measurements of their physical properties, as well for the development of devices. Various growth methods have been described for RE-123 (RE=Y or any lanthanides elements except Ce, Pr, Pm, and Tb) single crystals. One of them is the flux method introduced by Schneemeyer et al. [6] and Wang et al. [7], who used a CuO–BaO self-flux to grow $YBa_2Cu_3O_{7-\delta}$ single crystals. The main advantage of this method is the growth of lengthwise single crystals that are easily extracted from the solidified flux matrix.

In addition to good electrical and magnetic properties, candidates for technological applications must have good mechanical performance. The mechanical properties of high-temperature superconductors can be improved by several procedures. One of them is the addition of Ag, which reduces pores and cracks in the microstructure [8, 9], resulting in higher tensile and bending strengths [10] and increased microplasticity [11]. Another, applicable to melt-textured samples, is the incorporation of particles of the Y_2BaCuO_5 phase and Ag doping of the matrix, which increases hardness, elastic modulus, and resistance to fracture [8, 12, 13].

A previous work succeeded to grow single crystals of $REBa_2Cu_3O_{7-\delta}$ superconductors from rare-earth oxides extracted from xenotime ore [3]. The measured hardness and elastic modulus were similar to those of fully oxygenated $YBa_2Cu_3O_{7-\delta}$ single crystals and of melt-textured $YBa_2Cu_3O_{7-\delta}$. We were surprised by this finding, since we expected the doping with the different ion species from the xenotime mineral to strengthen the $REBa_2Cu_3O_{7-\delta}$ single crystals. The single crystals prepared from the xenotime mixture should, therefore, exhibit higher hardness than pure $YBa_2Cu_3O_{7-\delta}$ single crystals or melt-textured $YBa_2Cu_3O_{7-\delta}$. Reference [3] suggested that indentation fractures might affect the hardness in the ab-plane, but presented no additional evidence to support the suggestion.

Driven by this unexpected finding and wishing to check the proposed explanation, we here investigate in greater detail the mechanical properties (hardness, elastic modulus, and indentation fracture toughness) of $REBa_2Cu_3O_{7-\delta}$ single crystals with instrumented indentation testing. We examine the active slip systems and the variation of mechanical properties for different crystallographic orientations and apply theoretical modeling of the hardness anisotropy to understand the possible influences of solid solution hardening and indentation fracture on hardness.

2 Experimental Procedure

The chemical procedure yielding the natural mixture of trivalent rare-earth oxides RE_2O_3 from xenotime minerals is detailed elsewhere [5]. Large $REBa_2Cu_3O_{7-\delta}$ single crystals resulted from a CuO–BaO self-flux method similar to that described by Schneemeyer et al. [6] and Wang et al. [7]. The main advantage of this method is that it grows single crystals lengthwise, which are moreover easily extracted from the solidified flux matrix.

The starting material was a powder mixture of RE_2O_3, $BaCO_3$ (99.9 % purity) and CuO (99.99 %) at a molar ratio of 1RE.4Ba.10Cu. The starting mixture, therefore, had a relative excess of Ba and Cu in comparison to the final desired composition of $REBa_2Cu_3O_{7-\delta}$. The mixture was ground for 4 h in a ball mill and then placed in a ZrO_2 crucible that was heated up to 980 °C at a 100 °C/h rate in air. After 1 h at the final temperature, the samples were slowly cooled (3 °C/h) to 880 °C and then cooled in a furnace to room temperature. At the end of this process, the grown single crystals were extracted and oxygenated at 420 °C for 5 days in flowing O_2 atmosphere to yield the superconductive orthorhombic structure. Large single crystals resulted, with typical size $3 \times 3 \times 0.03$ mm^3, and were characterized by XRD, SEM, and electrical resistivity. The results of the characterization were described elsewhere [5].

Hardness (H) and elastic modulus (E) profiles were determined using a Nanoindenter XP™ with a diamond Berkovich indenter, following the Oliver and Pharr's method [14]. The indentations were performed in ten loading–unloading cycles up to a maximum load of 400 mN. Several indentations were performed in different samples and at different regions of each, to check for sample homogeneity. Given the small available surface, each sample was indented along grids of 3×3 or 2×2 at several places. The indentations were separated by at least 50 μm.

To reveal the effect of load on the resulting fracture pattern, numerous indentations were made at different loads with a cube corner indenter on the ab-plane. The crack pattern was observed in SEM images using backscattered or secondary electrons.

The room temperature indentation fracture toughness K_C was measured with a diamond cube corner indenter at single loading/unloading cycles. The maximum load was 400 mN. K_C was calculated from the relation proposed by Harding et al. for a cube corner indenter [15]:

$$K_c = \alpha \cdot \sqrt{\left(\frac{E}{H}\right)^{\frac{1}{2}} \cdot \frac{P}{c^{\frac{3}{2}}}} \qquad (1)$$

where c is the radial crack length, P is the applied load, and the prefactor is a constant, $\alpha = 0.036 \pm 0.014$. The crack lengths were measured by optical microscopy and SEM

immediately after the indentations tests, in order to avoid deleterious chemomechanical effects [16–18].

The initial stages of deformation and fracture in the indentation process were also investigated by means of single loading–unloading cycles with a cube corner indenter at a load of 20 mN, to avoid the extensive cracking that occurs at higher loads. The cube corner indenter promotes cracking at smaller loads than the Berkovich indenter and induces much higher strains. The dependence on crystallographic orientation was investigated by rotating the sample from 0° to 60° at 15° steps between tests. At least 15 indentations were performed for each orientation. With the cube corner indenter, the hardness was calculated from the ratio P/A, where P is the maximum load and A the projected area of the hardness impression. A is calculated from the contact depth h_c as a polynomial function $C_0 h_c^2 + C_1 h_c + C_2 h_c^{1/2} + \dots$ where C_i are constants; for a perfect cube corner indenter, $A = 2.598\ h_c^2$. The elastic modulus was also calculated from the initial unloading curve by the Oliver–Pharr method, using 50 % of the unloading curve. The area function of both the Berkovich and the cube corner indenters and frame compliance were calibrated using a standard fused silica sample. The [100] and [010] directions on the ab-plane were determined from the observation of the orientation of the growth steps on the sample surface.

3 Results

Figure 1 shows typical loading–unloading curves for a Berkovich tip indenter applied on the ab-plane. Contact depths between 2,200 nm and 2,800 nm are obtained at a load of 400 mN. Several discontinuities are observed along the curve, especially at contact depths approximately greater

than 600 nm. These discontinuities are associated with crack nucleations parallel to the surface and are nucleated at different loads as shown by pictures b and c in Fig. 1, with the cracks sometimes being large, as highlighted in Fig. 1b. Due to the lamellar structure of the $REBa_2Cu_3O_{7-\delta}$ structure, these are lateral cracks that, once nucleated, promote detachment of the material under the indenter (chipping). The indenter then loses support, and a discontinuity takes place in the loading curve.

Figure 2 shows slip lines parallel to the [100] and [010] directions inside the indentations. These traces, reminiscent of the [100](001) and [010](001) slip systems reported in the literature for $YBa_2Cu_3O_{7-\delta}$ single crystals [19, 20], indicate that the slip systems for $REBa_2Cu_3O_{7-\delta}$ and for $YBa_2Cu_3O_{7-\delta}$ are the same. These slip systems produce no slip lines on the ab-plane, to which they are parallel; yet, they do produce slip lines inside the indentations.

Figure 3a and b show the hardness and elastic modulus profiles, respectively, as functions of the contact depth. The hardness is 7.4 GPa near the surface and remains constant up to a contact depth of approximately 600 nm. At larger depths, hardness decreases, reaching a minimum of 4.6 GPa at maximum contact depth. The elastic modulus decreases continuously from 177 GPa near the surface to 115 GPa at a depth of 600 nm and reaches 60 GPa at the maximum contact depth.

Although the hardness may decrease with increasing indentation depth due to the indentation size effect [21], the reduction of the elastic modulus was unexpected. In search of more information, we measured the area of each Berkovich indentation from the SEM photographs and divided the load of 400 mN by the measured area to calculate the hardness at maximum depth. When the resulting hardness was compared with that obtained by instrumented indentation, agreement was found. This shows that the low hardness at

Fig. 1 **a** Typical loading–unloading curves of a Berkovich indentation in the ab-plane of a $REBa_2Cu_3O_{7-\delta}$ single crystal showing tip incursions during loading associated with crack nucleation. Indentation cracking associated with loading curves represented by **b** *open* and **c** *solid symbols* are displayed
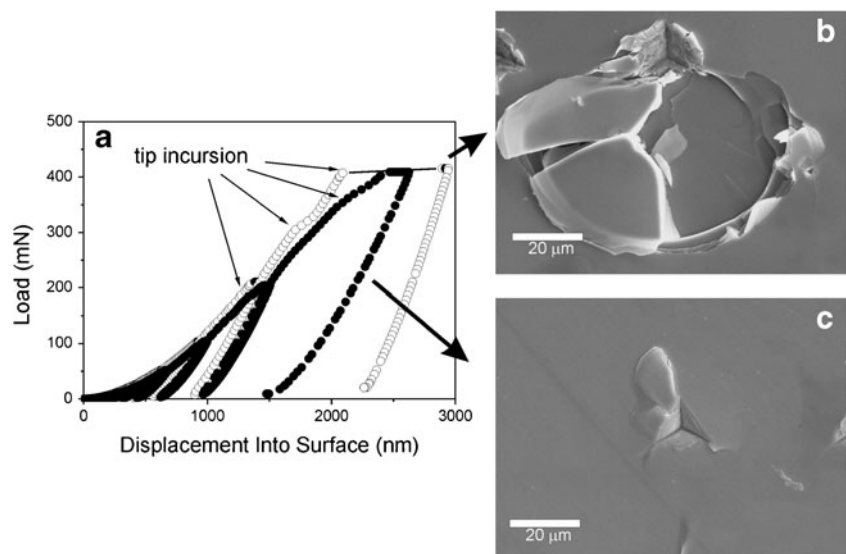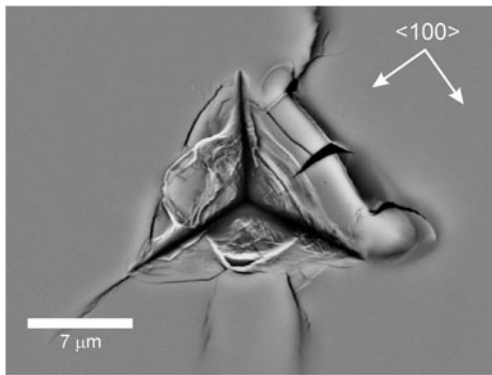
Fig. 2 SEM of a 400 mN Berkovich indentation on the *ab*-plane. Slip lines inside the indentation corresponds to the traces of the [100](001) and [010](001) slip systems

to affect the measured contact stiffness and the calculated elastic modulus as well.

Figure 4 surveys the cracking dependence on load for the cube corner indenter. Micrographs a, b, and c show the cracking patterns for 20 mN, 200 mN, and 400 mN, respectively. At 20 mN, well-delineated radial cracks aligned along the indenter diagonals are visible [Fig. 4a]. Material is also displaced at the edges of the imprint. The displacement appears to be lamellar, following the lamellar crystal-line structure of the orthorhombic unit cell. As the load increases, the damage grows around the indentation. Lateral cracks appear and their extent increases with the load. At 200 mN [Fig. 4b], they interfere so much with the radial cracks that the indentation fracture toughness can no longer

maximum depth characteristic of $ReBa_2Cu_3O_{7-\delta}$ single crystals is due to nucleation and propagation of lateral cracks at loads above a certain threshold. These cracks are expected
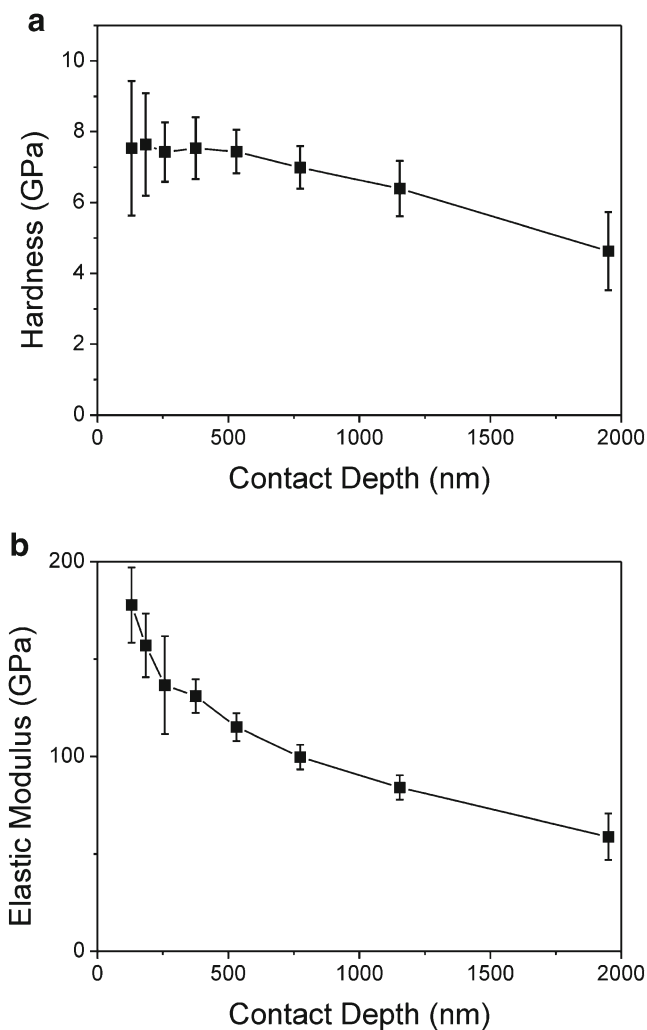

Fig. 3 **a** Hardness and **b** elastic modulus as a function of contact depth for *ab*-plane of $REBa_2Cu_3O_{7-\delta}$ single crystal using a Berkovich indenter
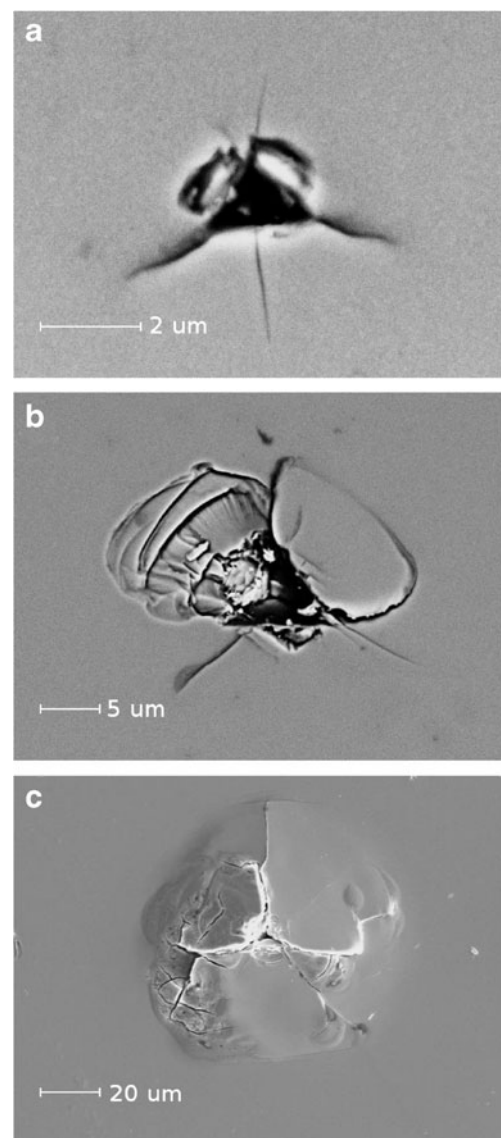
Fig. 4 SEM micrographs of cube corner indentations on *ab*-plane of $REBa_2Cu_3O_{7-\delta}$ single crystal with loads of **a** 20 mN, **b** 200 mN, and **c** 400 mN

be calculated from the radial lengths. At the maximum load of 400 mN [Fig. 4c], the damage is so severe that lateral cracks propagate parallel to the surface, around the entire indentation impression, extending beyond the radial cracks and promoting chipping.

As the radial cracks are poorly defined at high loads, our estimate of the indentation fracture toughness of the ab-plane of single crystals was obtained from loads up to 100 mN. Table 1 shows the indentation fracture toughness K_C calculated using Eq. 1 as well as the average crack length c for each load. The indentation fracture toughness is constant, i.e., independent of the load, $K_c = 0.8 \pm 0.2$ MPa m$^{1/2}$.

Figure 5 shows the anisotropy in the mechanical properties. The hardness and elastic modulus measured with a cube corner indenter are plotted as functions of the orientation θ of the cube corner indenter diagonal relative to the assumed [100] direction in the ab-plane. Within the experimental error, both H and E are independent of the crystallographic orientation. The measured hardness is approximately 9 GPa and the elastic modulus, 160 GPa. This hardness is slightly higher than and the elastic modulus is approximately the same as the hardness and the elastic modulus measured by the Berkovich indenter, respectively. Different hardness have been reported for a few materials, depending on whether the measurements are made with a Berkovich or a cube corner indenter [22]. Even in those cases, however, the two indenters yield the same elastic modulus.

Figure 6 shows the plastic deformations around the indentations for various directions of the cube corner diagonals on the ab-plane. The anisotropy in plastic deformation around the indentation is evident, although the measurements showed no anisotropy in the hardness and elastic modulus. We observed two slip directions perpendicular to each other at the surface. These coincide with the <100> directions, which corresponds to the activation of the [100] (001) and [010](001) slip systems observed in YBa$_2$Cu$_3$O$_{7-\delta}$ single crystals and are indicated by arrows in Fig. 6a, b, d and e. No slip lines are observed because these slip systems are parallel to the ab-plane. Radial cracks partially aligned with the indenter diagonals along the <110> and <100> directions are also seen. Reports in the literature indicate that the primary crack plane is along the {100} planes for YBa$_2$Cu$_3$O$_{7-\delta}$ single crystals [23, 24].

Table 1 Cube corner indentation load, crack length, and indentation fracture toughness as calculated using Eq. 1. The values of H and E used were 7.5 GPa and 142 GPa, respectively

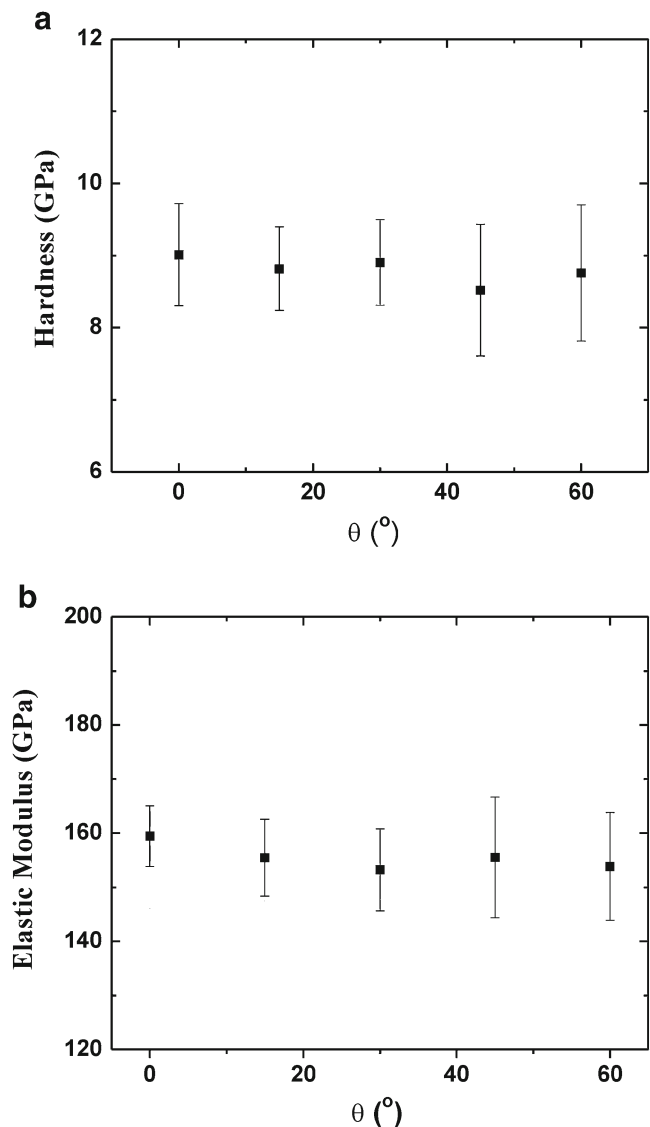| P (mN)	c (µm)	K_C (MPa m$^{1/2}$)
20	2.8±0.3	0.7±0.1
50	4.7±0.7	0.8±0.2
100	8±1	0.8±0.2

Fig. 5 **a** Hardness and **b** elastic modulus measured using a cube corner indenter as a function of the diagonal orientation of the cube corner indenter for the ab-plane of REBa$_2$Cu$_3$O$_{7-\delta}$ single crystal

Figure 6c and e show lateral detachment of material around the indentation, possibly a result of lateral crack nucleation.

4 Discussion

The hardness measured with the Berkovich indenter, 7.4 ± 0.2 GPa, is approximately constant near the surface. For contact depths greater than 600 nm, the hardness decreases continuously to 4.6 GPa at the maximum depth. The elastic modulus also decreases continuously from 177 GPa near the surface to 60 GPa at maximum depth. Several discontinuities in the loading curve were observed for indentation depths greater than 600 nm, associated with the nucleation of lateral cracks. These cracks affect the measurement of

Fig. 6 SEM photograph of 20 mN cube corner indentations on the *ab*-plane and with one of the indenter diagonals aligned at **a** 0°, **b** 15°, **c** 30°, **d** 45°, and **e** 60° from the <100>directions indicated by *arrows*
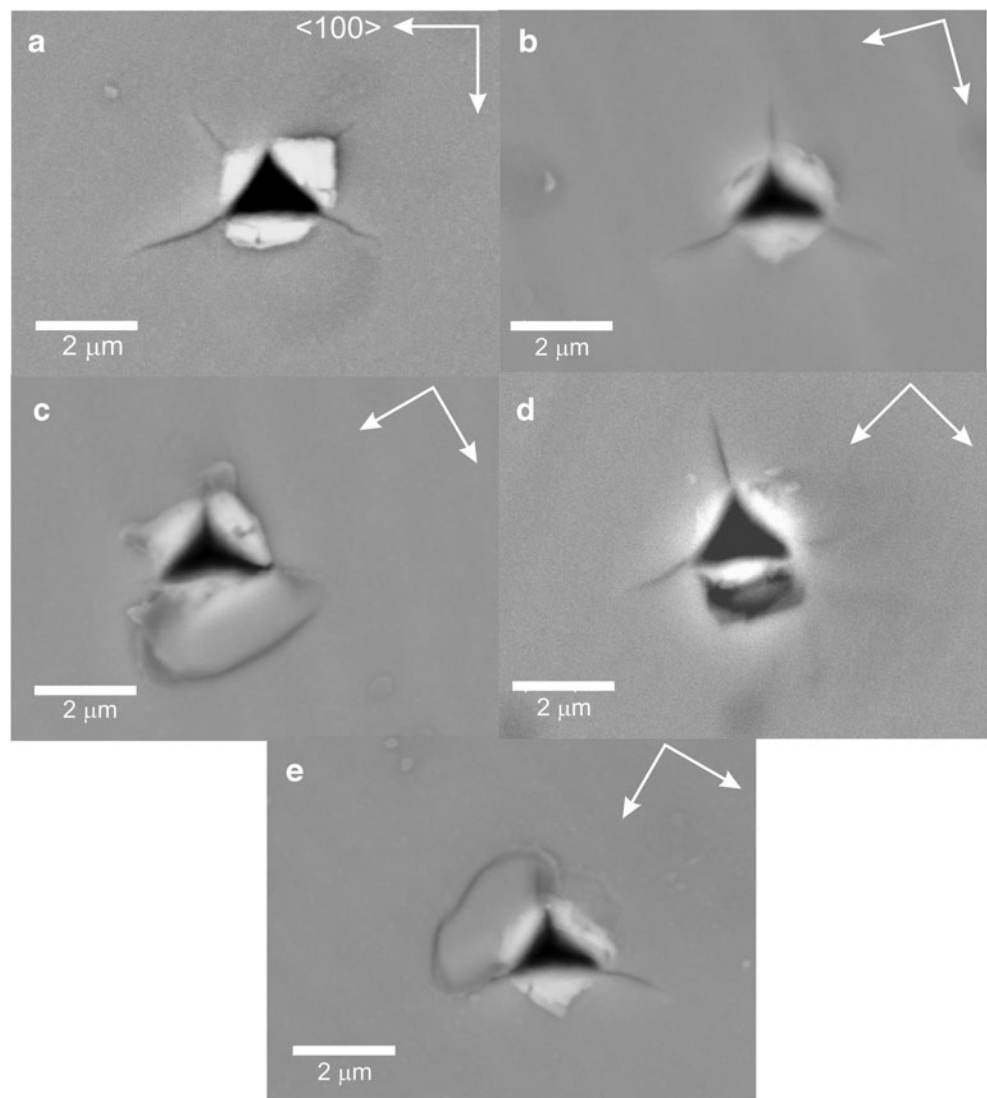
hardness and elastic modulus in two ways: (a) as the crack is nucleated, material is displaced and the indenter penetrates deeper into the material and (b) the contact stiffness changes from the value measured at the beginning of the unloading cycle and reduces the calculated elastic modulus. Evidence favoring these two conclusions is provided by the instrumented indentation measurements and direct measurements of the hardness, which yield the same result.

Table 2 compares the hardness and elastic modulus of various superconductor systems with different microstructures and compositions. As a rule, polycrystalline samples have lower hardness than melt-textured and single-crystal samples, a difference attributed to pores. The hardness of melt-textured samples is higher due to the lower porosity and the presence of the RE-211 phase. The hardness of the *a*(*b*)*c*-plane is slightly lower than that of the *ab*-plane. Our result for the hardness is in the 7–11 GPa range measured by instrumented indentation on *ab*- or *a*(*b*)*c*-planes of melt-textured Y-123 samples [25, 26] and only slightly lower

than the 8.5 ± 0.5 GPa value previously reported for the *ab*-plane of $REBa_2Cu_3O_{7-\delta}$ single crystals [5]. Our result also agrees with the hardness of approximately 8.6 GPa measured on Ru-1212 polycrystalline samples, a material with structure very similar to $YBa_2Cu_3O_{7-\delta}$ [27]. $REBa_2Cu_3O_{7-\delta}$ single crystals contain small amounts of Dy, Ho, and Er dissolved in their structures [5], probably in substitutional solid solution to Y. The ionic radii of Dy, Ho, and Er are 0.912 A, 0.901 A, and 0.881 A, respectively. The ionic radius of Y is 0.9 A. Consequently, due to the larger ionic radii, Dy and Er ions tend to distort the lattice, generate stresses, and increase the barrier for dislocation motion. We expected these ions to increase the hardness of $REBa_2Cu_3O_{7-\delta}$ single crystals by solid solution strengthening.

The hardness are nevertheless the same, which indicates that another mechanism may be at work. We, therefore, go back to Fig. 1. The micrographs show extensive lateral microcracks due to the lamellar structure of the $REBa_2Cu_3O_{7-\delta}$. These cracks are probably nucleated at very small loads and

Table 2 Hardness and elastic modulus from the literature for different high-temperature superconductor samples

Sample	H (GPa)	E (GPa)
Polycrystalline Y-123[13]	3.4 ± 0.7	125 ± 10
Polycrystalline Y-123 doped with Ag [13]	3.2 ± 0.6	140 ± 10
Polycrystalline RE-123[7]	5.0 ± 2	133 ± 15
Polycrystalline $RuSr_2GdCu_2O_{8+d}$[12]	9 ± 2	150 ± 30
ab-Plane of melt-textured Y-123[11]	8 ± 1	170 ± 10
$a(b)c$-plane of melt-textured Y-123[11]	6.9 ± 0.3	160
ab-Plane of melt-textured Y-123 doped with Ag[11]	8 ± 1	140–220
$a(b)c$-Plane of melt-textured Y-123 doped with Ag[11]	7.1 ± 0.8	140–180
ab-Plane of melt-textured RE-123[7]	9.0 ± 0.5	206 ± 10
$a(b)c$-Plane of melt-textured RE-123[7]	9.0 ± 0.5	190 ± 10
ab-Plane of melt-textured $Y_{0.95}Er_{0.05}Ba_2Cu_3O_{7-\delta}$[10]	7.4 ± 0.6	158 ± 4
$a(b)c$-Plane of melt-textured $Y_{0.95}Er_{0.05}Ba_2Cu_3O_{7-\delta}$[10]	7.2 ± 0.3	176 ± 6
ab-Plane of RE-123 single crystals[6]	8.5 ± 0.5	143 ± 3
ab-Plane of $YBa_2Cu_3O_7$ single crystals[15]	–	182
$a(b)c$-Plane of $YBa_2Cu_3O_7$ single crystals[15]	–	143

displace material underneath the indenter. The displacement allows larger tip penetration depths and reduces contact stiffness. While the deeper penetration decreases the hardness in proportion to $1/h_c^2$, where h_c is the contact depth, the reduced contact stiffness increases hardness in proportion to h_c [14]. The overall result is a reduction in hardness with increasing penetration depth, which may explain the equivalent hardness of $REBa_2Cu_3O_{7-\delta}$ and $YBa_2Cu_3O_{7-\delta}$ single crystals.

The continuous decrease in the elastic modulus with contact depth, as well as its low value at large depths in comparison with literature data are attributed to crack nucleation by indentation. The elastic modulus measured at low loads up to a depth of 200 nm is in the 135–175 GPa range, in agreement with values reported in previous studies: the elastic modulus was in the 160–175 GPa range for melt-textured $Y_{0.95}Er_{0.05}Ba_2Cu_3O_7$ and in the 150–220 GPa range for melt-textured Y-123 samples doped with Ag [25], in the 160–170 GPa range for pure Y-123 melt-textured samples [26], and close to 125 GPa for pure polycrystalline samples [28]. The range found in our study agrees with the 143 ± 3 GPa value found in an earlier study of the ab-plane of $REBa_2Cu_3O_{7-\delta}$ single crystals [5]. The elastic modulus of Ru-1212 polycrystalline samples lies near 145 GPa [27].

The indentation fracture toughness of our samples, 0.8 ± 0.2 MPa m$^{1/2}$, is consistent with published toughness measured by the indentation technique for high-temperature superconductors samples with different microstructures [13, 25, 26, 29]. The toughness of the ab-plane of melt-textured $REBa_2Cu_3O_{7-\delta}$ samples was found to be in the 0.8–1.2 MPa m$^{1/2}$ range [26]. Measurements of K_C in both the ab- and $a(b)c$-planes of melt-textured $Y_{0.95}Er_{0.05}Ba_2Cu_3O_{7-\delta}$ samples yielded values of $1.3\pm$ 0.3 and 0.8 ± 0.2 MPa m$^{1/2}$, respectively [25]. Measurements in Ag-doped melt-textured Y-123 gave higher values, in the 1.4–1.6 MPa m$^{1/2}$ range for both ab- and $a(b)c$-planes; the doping raises K_c because Ag fills pores and cracks in the microstructure. Fracture toughness measured by other methods such as using single-edge notch bend (SENB) samples are near 1 MPa m$^{1/2}$ for undoped samples [13]. The fracture toughness for the ab- and $a(b)c$-planes are 0.8 and 0.32 MPa m$^{1/2}$, respectively [29].

Foerster et al. [30] compared the mechanical properties of samples with different microstructures produced from elements extracted from xenotime. The melt-textured samples gave the highest measured hardness and elastic modulus because their microstructures contain 211 inclusions and pores embedded in the 123 matrix. The highly porous polycrystalline sample showed the lowest hardness. The indentation fracture toughness for melt-textured samples was found to be in the 0.7–1.0 MPa m$^{1/2}$ range reported in the literature. It was concluded that melt-textured $REBa_2Cu_3O_{7-\delta}$ samples have the most favorable mechanical properties for technological applications.

We found H and E did not change with crystallographic orientation in the ab-plane within experimental error, an indication that the mechanical properties are not strongly dependent on the orientation. Plastic deformations nonetheless showed anisotropy. To understand this discrepancy better, we studied stress and hardness dependence on the indenter orientation on the basis of the model of Brookes et al. [31]. According to this model, the hardness anisotropy is determined by the active slip systems accommodating plastic deformations in the hardness test by means of dislocation motion. Materials with the same active slip systems show similar anisotropic hardness.
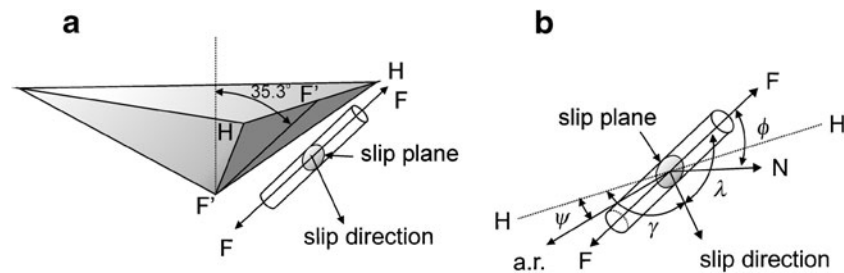
Fig. 7 **a** Schematic representation of a slip system and its orientation with respect to the face of a cube corner indenter and **b** the definition of the angles used in Eq. 2 to calculate the resolved shear stress acting on the slip system. *HH* direction of the edge of the particular indenter face, *F′F′* direction of the steepest slope of the indenter face, *FF* stress axis, *N* direction normal to the slip plane and *a.r.* rotation axis of the slip system

The model assumes that (a) the maximum tensile stress acting on the displaced material is along an axis parallel to the steepest slope along the face of the indenter, represented by the *F′F′* direction in Fig. 7a; (b) the slip system may rotate, which favors activation; (c) slip systems able to rotate about an axis parallel to indenter face and the surface is most favorably activated (when the directions a.r. and HH are coincident in Fig. 7b, and $\psi=0$); and (d) the maximum constraint on rotation of the slip system occurs for slip direction coincident with the HH direction [$\gamma=0$ in Fig. 7b].

According to this model, the effective resolved shear stress (ERSS) τ_e on a particular slip system is:

$$\tau_e = \frac{1}{2}\left(\frac{F}{A}\right)\cos\lambda.\cos\phi.(\cos\psi + \sin\gamma) \qquad (2)$$

where F is the applied load, A is a cross-sectional area, λ is the angle between the slip direction and the stress axis considered as the steepest slope of an indenter face, ϕ is the angle between the normal to the slip plane and the stress axis, ψ is the angle between the axis of rotation of the slip system and a direction parallel to the indenter face and the surface defined by HH, and γ is the angle between the slip direction and HH, as shown in Fig. 7a and b. The term $\cos\lambda \cdot \cos\phi$ stems from the projection of the maximum tensile stress along FF on the slip plane and slip direction and the term ($\cos\psi+\sin\gamma$), from the slip system rotation relative to the HH direction, as described in the preceding paragraph.

The ratio *F/A*, which describes the maximum stress parallel to the indenter face, is not the material hardness. Therefore, we define a normalized ERSS as the ratio $\tau_e/(F/A)$, the computation of which yields the relative magnitudes of the shear stresses on different slip systems as a function of the indenter diagonal on a particular crystal plane. The directions with the highest shear stresses are the ones with the lowest hardness.

The observed slip systems are the same as those for Y-123 samples: (001) planes with [100] and [010] Burgers vectors [19, 20]. For a given orientation θ of the indenter on the *ab*-plane, we used vector calculus to compute the ERSS using Eq.
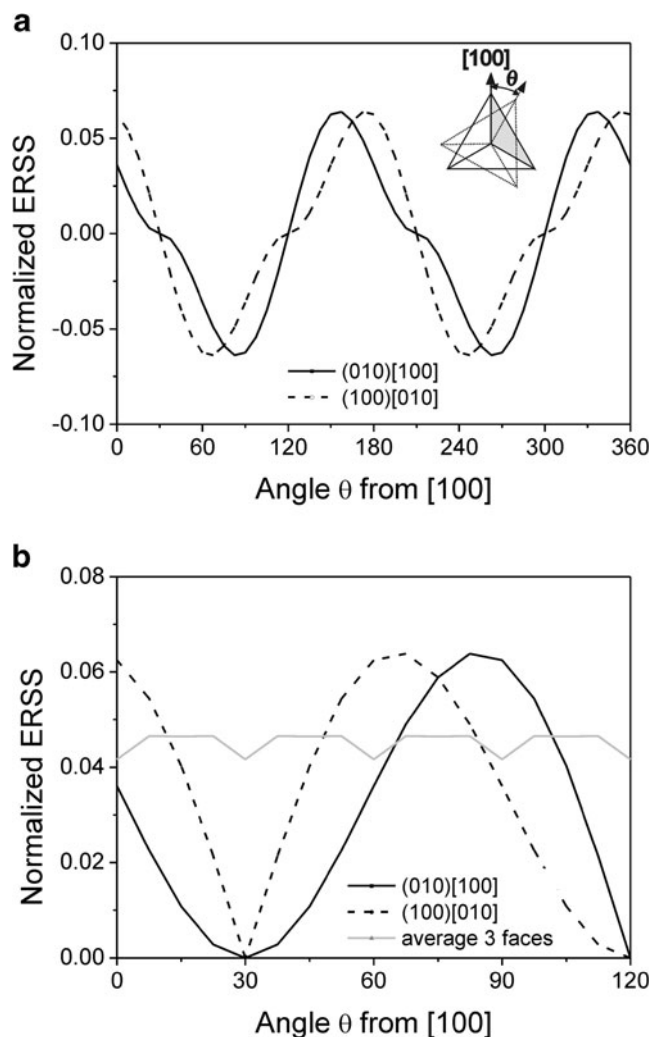

Fig. 8 **a** Normalized effective resolved shear stress calculated using Eq. 2 for the slip systems of YBa$_2$Cu$_3$O$_{7-\delta}$ on a single face of a cube corner indenter (the indenter *gray face* shown in the *inset*) and **b** average normalized effective resolved shear stress of the three faces of a cube corner indenter on the *ab*-plane as a function of the diagonal orientation

2 for given indenter face for both slip systems. The angle between one of the faces of the cube corner indenter and the central axis is 35.3° as shown in Fig. 7a.

Figure 8a shows the normalized ERSS calculated for the two slip systems on a single face of a cube corner indenter (gray face in the inset) as it rotates from the [100] direction on the ab-plane. Both slip systems operate simultaneously. The axis of rotation of the two slip systems is always perpendicular to the ab-plane. Therefore, the angle ψ is always 90° and $\cos\psi$ is zero in Eq. 2. The ERSS is, hence, solely determined by the resolved shear stresses on the slip system and by its ability to rotate, due to the term $\sin\gamma$. When the direction HH of a face of the indenter coincides with one of the slip directions [100] or [010], the ERSS is zero. Shear stresses are zero at $\theta=30°$, 120°, 210°, and 300°. This can be seen in Fig. 6c, as the material is less displaced at the face with zero stress.

Figure 8b shows the average normalized ERSSs. Here we consider the maximum shear stress on each of the three faces of the cube corner indenter. For comparison, the absolute stresses on the slip systems are also plotted, a single face considered for comparison. The average shear stress is insensitive to changes in the orientation, a result that is easily understood, since the shear stress is low, or even zero, on one face when the stresses are high on the other faces. Simulations for a Berkovich indenter resulted in the resolved shear stress curves with the same profile, although with higher values. The calculations confirm the inexistence of hardness anisotropy on the ab-plane. The observed hardness anisotropy is consistent with the activation of (001)[100] and (001)[010] slip systems for REBa$_2$Cu$_3$O$_{7-\delta}$ single crystals, which coincide with the slip systems for YBa$_2$Cu$_3$O$_{7-\delta}$ single crystals.

5 Conclusions

The mechanical properties of the ab-plane of high-temperature REBa$_2$Cu$_3$O$_{7-\delta}$ superconductor were characterized by instrumented indentation. The measured hardness and elastic modulus were 7.4 ± 0.2 GPa and in the range 135–175 GPa at small depths, respectively. Increased loads promote crack nucleation that decreases the measured hardness and elastic modulus at larger depths. An indentation fracture toughness of 0.8±0.2 MPa m$^{1/2}$ was measured from the radial crack length resulting from cube corner indentations. The hardness and elastic modulus depend weakly on the crystallographic orientation on the ab-plane. Theoretical modeling associated the activation of the (001)[100] and (001)[010] slip systems with the observed slip lines in the ab-plane and the hardness anisotropy. REBa$_2$Cu$_3$O$_{7-\delta}$ and

YBa$_2$Cu$_3$O$_{7-\delta}$ single crystals have the same slip system. Evidence of cracking along the {100} and {110} planes on the ab-plane was found. The similar hardness of the REBa$_2$Cu$_3$O$_{7-\delta}$ and YBa$_2$Cu$_3$O$_{7-\delta}$ compounds were found to be due to the same operative active slip systems and to the effect of lateral cracking during indentation, which counterbalances the expected solid solution strengthening resulting from the contribution of different ion species from the xenotime mineral to the REBa$_2$Cu$_3$O$_{7-\delta}$ single crystals.

References

1. Critical Materials Strategy (2010) 97, US Department of Energy
2. C.R. Neary, D.E. Highley, in *Rare Earth Element Geochemistry*, ed. by P. Henderson (Elsevier, Amsterdam, 1984)
3. P. Rodrigues Jr., A.R. Jurelo, J. Flemming, Mod. Phys. Lett. **13**, 485 (1999)
4. A.R. Jurelo, P. Rodrigues Jr., A.E. Carrillo, T. Puig, X. Obradors, J. Barbosa, Physica C **399**, 87 (2003)
5. A.R. Jurelo, J. Flemming, F.C. Serbena, C.R. Carubelli, P. Rodrigues Jr., C.E. Foerster, F.T. Dias, J. Cryst. Growth **311**, 3539 (2009)
6. L.F. Schneemeyer, J.V. Waszczak, T. Siegrist, R.B. van Dover, L.W. Rupp, B. Batlogg, R.J. Cava, D.W. Murphy, Nature **328**, 601 (1987)
7. Y. Wang, L.W.M. Schreurs, P. Van der Linden, Y. Li, P. Bennema, J. Cryst. Growth **106**, 487 (1990)
8. F. Tancret, I. Monot, F. Osterstock, Mater. Sci. Eng. A **298**, 268 (2001)
9. T. Miyamoto, K. Nagashima, N. Sakai, M. Murakami, Physica C **340**, 41 (2000)
10. N. Sakai, S.J. Seo, K. Inoue, T. Miyamoto, M. Murakami, Physica C **335**, 107 (2000)
11. L.K. Markov, T.S. Orlova, N.N. Peschanskaya, B.I. Smirnov, Y.P. Stepanov, V.V. Shpeizman, Phys. Solid State **45**, 1629 (2003)
12. J.J. Roa, X.G. Capdevila, M. Martínez, F. Espiell, M. Segarra, Nanotechnology **18**, 385701 (2007)
13. F. Yeh, K.W. White, J. Appl. Phys. **70**, 318 (1991)
14. W.C. Oliver, G.M. Pharr, J. Mater. Res. **7**, 1564 (1992)
15. D.S. Harding, W.C. Oliver, G.M. Pharr, Mater. Res. Soc. Symp. Proc. **356**, 663 (1995)
16. R.P. Vasquez, B.D. Hunt, M.C. Foote, Appl. Phys. Lett. **53**, 2692 (1988)
17. R. Argyropoulou, M. Ochsenkühn-Petropoulou, C. Dounis, P. Karaboulis, A. Altzumailis, K.M. Ochsenkühn, J. Mater. Process. Technol. **181**, 2 (2007)
18. J.D. Tatum, J.W.H. Tsai, M. Chopra, S.W. Chan, J.M. Phillips, S.Y. Hou, J. Appl. Phys. **77**, 6370 (1995)
19. M. Verwerft, D.K. Dijken, J.T. De Hosson, A.C. Van der Steen, Phys. Rev. B **50**, 3271 (1994)
20. J. Zheng, Q. Li, D. Feng, S. Ding, S. Yu, G. Shen, F. Liu, L. Zhou, H. Mou, J. Appl. Phys. **72**, 4634 (1992)
21. W.D. Nix, H. Gao, J. Mech. Phys. Solids **46**, 411 (1998)
22. T. Chudoba, P. Schwaller, R. Rabe, J.-M. Breguet, J. Michler, Phil. Mag. **86**, 5265 (2006)
23. R.F. Cook, T.R. Dinger, D.R. Clarke, Appl. Phys. Lett. **51**, 454 (1987)

24. A.S. Raynes, S.W. Freiman, F.W. Gayle, D.L. Kaiser, J. Appl. Phys. **70**, 5254 (1991)
25. L.B.L.G. Pinheiro, A.R. Jurelo, F.C. Serbena, P. Rodrigues Jr., C.E. Foerster, A.L. Chinelatto, Physica C **470**, 465 (2010)
26. C.E. Foerster, E. Lima, P. Rodrigues Jr., F.C. Serbena, C.M. Lepienski, M.P. Cantão, A.R. Jurelo, X. Obradors, Braz. J. Phys. **38**, 341 (2008)
27. L.B.L.G. Pinheiro, F.C. Serbena, C.E. Foerster, P. Rodrigues Jr., A.R. Jurelo, A.L. Chinelatto, J.L.P. Júnior, Physica C **471**, 179 (2011)
28. P. Azambuja, P. Rodrigues Jr., A.R. Jurelo, F.C. Serbena, C.E. Foerster, R.M. Costa, G.B. Souza, C.M. Lepienski, A.L. Chinelatto, Braz. J. Phys. **39**, 638 (2009)
29. I.A. Parinov, *Microstructure and Properties of High-Temperature Superconductors*. (Springer-Verlag Berlin, 2007)
30. C.E. Foerster, F.C. Serbena, A.R. Jurelo, T.R. Ferreira, P. Rodrigues Jr., A.L. Chinelatto, IEEE T. Appl. Supercon. **21**, 52 (2011)
31. A.C. Brookes, J.B. O'Neill, B.A.W. Redfern, Proc. Roy. Soc. Lond. A. **322**, 73 (1991)